



OPEN Study on energy absorption characteristics of the corrugated straight tube flip type energy absorption device

Jianzhuo Zhang¹, Fengnian Zhao^{1✉}, Hao Guo¹, Chuanxu Wan¹ & Yonghui Xiao²

To rapidly dissipate impact energy during a rockburst and safeguard support equipment from damage, this study introduced a corrugated straight tube flip-type energy absorption device. The energy absorption characteristics of this device were analyzed through numerical simulation, and the theoretical formula for axial load was derived using an energy method. Based on the response surface design method, a predictive model for response values was established. The influence of structural parameters on these response values was analyzed, leading to the determination of optimal structural parameters in conjunction with the application frame type and response value optimization objectives. Numerical simulations and impact tests were conducted and compared. The optimal structural parameters determined were: basic circle radius of 80 mm, inner convex arc radius of 23 mm, thickness of 6.5 mm, and curling radius of 13 mm. The impact test results indicated that the initial peak value of the support reaction force was 2710.91 kN, which fell within the range of 1.2–1.5 times the working resistance. The average support reaction force was larger, at 3028.10 kN, with a maximum energy absorption of 349.89 kJ. Comparing these results with numerical simulations revealed an error rate of less than 10%, demonstrating high consistency between simulation and test outcomes. The impact test confirmed that the corrugated straight tube flip-type energy absorption device exhibited excellent energy absorption and anti-impact characteristics.

Keywords Rock burst, Energy absorption device, Corrugated straight tube, Energy absorption characteristic

Rock burst is a dynamic disaster of deep mining in coal mines^{1,2}. As mining depth increases, the occurrence conditions of coal seams become increasingly complex, and the mine ground stress and rock strength gradually increase^{3–5}. Under the influence of external mining disturbances, the elastic strain energy within coal and rock is released instantaneously, leading to shock failure of the coal and rock mass and the occurrence of rock burst disasters^{6–9}. In the past decade, 95% of rock bursts have occurred in roadways^{10,11}. When a rock burst occurs, the elastic strain energy inside the coal and rock is released instantly, often resulting in destructive phenomena such as roof subsidence, roof fall, rib spalling, floor heave, and overall section shrinkage in roadways^{12–14}. Hydraulic supports, serving as the supporting equipment for roadways, are widely used underground and play a crucial role in providing support^{15,16}. This type of support improves the impact resistance of the roadway support system to some extent and can generally withstand rock bursts with low energy release^{17,18}. However, when high-energy rock bursts occur, the impact load instantly exceeds the bearing capacity of the supports. The safety valve cannot successfully open to release pressure in a short period of time, leading to phenomena such as bending, tilting, or straight tube explosion of the pillars, and even the entire frame toppling over and the top and bottom beams bending^{19–22}. Therefore, how the support responds to impact pressure in a short time and mitigates its impact damage is a critical issue that needs to be addressed.

Based on this problem, Pan et al.²³ established a dynamic model for rock burst support and designed an energy-absorbing and anti-impact hydraulic support. When a rock burst occurs, the support resistance of the column increases instantaneously. If this resistance exceeds the activation threshold of the energy absorption device, the device consumes impact energy through its own buckling deformation, providing a certain displacement to mitigate the impact on the surrounding rock and protect the support equipment from damage. Therefore, the energy absorption device is crucial for the prevention and control of rock bursts. Experts and scholars have conducted extensive research on energy absorption devices. Ma et al.²⁴ designed a pre-folded

¹School of Mechanical Engineering, Liaoning Technical University, Fuxin 123000, People's Republic of China. ²School of Physics, Liaoning University, Shenyang 110036, People's Republic of China. ✉email: zhaofn1999@163.com

energy absorption component with a clear yield critical force and a reliable deformation mode. Xu et al.²⁵ proposed a new type of expansion-type energy-absorbing ejector rod. Taking the number of deformation zones and length of caliper section of ejector rod as design variables, the optimal design method of the expansion-type energy-absorbing ejector rod under different angles was obtained based on the response surface method. Wang et al.²⁶ designed a thin-walled circular tube vertical bar structure, conducted experimental verification, and optimized the model parameters based on experimental data. Yao et al.^{27,28} classified thin-walled multi-cell structures and materials (TWMCSM) in detail according to base materials and geometric features, describing the basic energy-absorption mechanisms and characteristics of TWMCSM. They proposed a bio-inspired multi-cell tube (BIMCT) with laterally-graded thickness and axially-graded aluminum foam filler. Parametric studies were conducted to explore the energy-absorption mechanism of BIMCT specimens, and a theoretical model was developed to predict the mean crushing force for BIMCT. Xiang et al.^{29–31} investigated the quasi-static compression characteristics of sandwich structures built with tapered tubes. The corrugation amplitude and the number of corrugations significantly influenced the energy-absorption parameters. Furthermore, the crashworthiness of corrugated tapered tubes under oblique loads was also examined. Based on previous studies, two types of laterally corrugated tapered tubes with variable thicknesses were designed, and their deformation patterns, load–displacement curves, and energy-absorption performance were analyzed. Xiao et al.³² proposed an aluminum foam-filled multi-cell square tube as an energy-absorption component, exploring the influence of the cross-sectional shape and the aluminum foam filling rate on the energy-absorption performance of the multi-cell square tube. Zhang et al.³³ studied the hexagonal periodic arrangement of energy-absorption structures, which reduced the stress and stress fluctuation of the column and effectively minimized the shape change of the weak link in the hydraulic support. Guo et al.³⁴ designed triangular, trapezoidal, and sinusoidal corrugated core energy-absorption structures. Through simulation analysis of the energy-absorption characteristic curves of the three corrugated core components, they concluded that the sinusoidal corrugated core showed the best energy-absorption effect in the single-layer corrugated element. Tian et al.³⁵ proposed a multi-cell thin-walled energy-absorption component with a mixed cross-section of circular and polygonal shapes, analyzed the influence of different structural parameters on the energy-absorption effect through axial crushing simulation, and used the NSGA-II genetic algorithm to determine the optimal structural parameters of the multi-cell thin-walled energy-absorption component. Pirmohammad et al.³⁶ investigated the effects of hole shapes and dimensions on the energy-absorption characteristics of square and octagonal bitubal structures, considering the impact of oblique loading on the deformation behavior of the holed structure. Gupta et al.³⁷ proposed a metallic thin-walled aluminum shell energy-absorption structure with a dome-cone combined geometry and analyzed its energy-absorption deformation mode by combining equivalent strain, equivalent strain rate, and nodal velocity distribution. Nikkhal et al.³⁸ proposed an energy-absorption structure composed of three thin-walled tubes with different geometric shapes stacked together in layers and analyzed the deformation modes and energy-absorption properties of different structures. Using a multi-criteria decision-making method, they determined that the multi-layer bio-inspired tube with square cross-sections and reinforcement walls exhibited better energy-absorption performance compared to all other designs. Baroutaji et al.³⁹ proposed sandwich tubes composed of thin-walled circular tubes and an aluminum foam core as energy absorption devices. The energy-absorption characteristics of the sandwich tubes were analyzed using finite element simulation, and the optimal configuration of the sandwich tube was determined using a multi-objective optimization method.

Existing research has contributed positively to the prevention and control of rock bursts; however, challenges persist, including low average bearing capacity and insufficient verification of energy absorption characteristics of devices under dynamic impact conditions. In this paper, a corrugated straight tube flip-type energy absorption device is proposed, employing circular tube flipping technology. This device dissipates impact energy through the deformation of the corrugated straight tube. Numerical simulations are used to analyze its energy absorption characteristics, and the interactions of key structural parameters on the device's response are examined. Based on the application framework, optimal structural parameters are identified, and numerical simulations and impact tests are conducted on the optimized device. The tests validate that the optimized energy absorption device demonstrates favorable energy absorption and anti-impact capabilities.

Structural design of the energy absorption device

The corrugated straight tube flip-type energy absorption device consists of a convex guiding platform, a corrugated straight tube, and a cover plate, as shown in Fig. 1. The convex guiding platform is a frustum of a

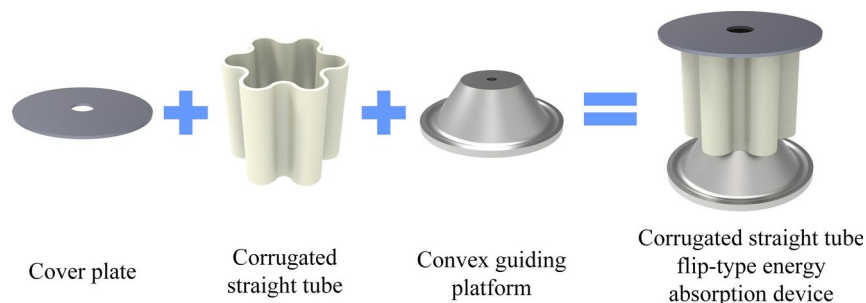


Fig. 1. Corrugated straight tube flip-type energy absorption device.

cone with a circular base, and the bottom of the frustum extends out an arc fillet surface. This design guides the corrugated straight tube to complete the flipping process more effectively. A screw threaded hole of a certain depth is processed at the center of the upper end face of the convex guiding platform, facilitating installation and handling. The corrugated straight tube is a circular tube with a corrugated section formed by six groups of alternating convex and concave arcs. Under axial load, the corrugated section circular tube exhibits a larger radial displacement compared to a plain circular tube of the same size during crushing deformation. This larger radial displacement results in greater bending resistance, ensuring that the corrugated straight tube does not crush before flipping and successfully completes the flipping process. The inner side of the bottom end face of the corrugated straight tube is rounded to reduce damage to the convex guiding platform during the downward movement of the tube. The fillet also ensures a smooth flipping process. The cover plate is a circular thin plate with a certain thickness. A circular through-hole is processed at the center of the cover plate, making it convenient for moving and disassembling the device. The cover plate and the corrugated straight tube are centrally aligned in the axial direction and are connected and fixed by welding. The upper end of the convex guiding platform is embedded within the inner part of the corrugated straight tube, with the rounded table surface being tangent to the inner surface of the corrugated straight tube. The end surface of the cover plate and the bottom end surface of the guiding platform are kept parallel and coaxial. The rounded surface and rounded corner surface of the convex guiding platform guide the cover plate and the bottom end of the corrugated straight tube to undergo stretching and flipping deformation.

The cross-sectional size of the corrugated straight tube is illustrated in Fig. 2. The inner convex arc of the corrugated straight tube has the same radius as the inner concave arc, and the convex arc is tangent to the concave arc.

The convex and concave arcs of the corrugated straight tube are alternately connected, with the number of convex and concave arcs being equal, both totaling six. Taking the center O of the basic circle of the corrugated straight tube as the reference, the angle α between the straight line passing through the center O_1 of the convex arc and the straight line passing through the center O_2 of the adjacent concave arc is $\alpha = 30^\circ$.

The base circle radius of the corrugated straight tube is denoted as R_b . The inner convex arc radius is denoted as R_c , and the inscribed circle radius is denoted as R_t . The distance between the center of the basic circle of the corrugated straight tube and the center of the concave arc is denoted as R_d . Since the radius of the inner convex arc of the corrugated straight tube is the same as that of the inner concave arc, the following relationship holds:

$$R_d = R_t + R_c \tag{1}$$

$$O_1O_2 = 2R_c \tag{2}$$

According to the Law of Cosines, the following equation can be derived:

$$(2R_c)^2 = R_b^2 + R_d^2 - 2R_bR_d \cos \alpha \tag{3}$$

Substituting $\alpha = 30^\circ$ and Eq. (1) into Eq. (3), R_t can be obtained as below:

$$R_t = \sqrt{4R_c^2 - \frac{1}{4}R_b^2} + \left[\frac{\sqrt{3}}{2}R_b - R_c \right] \tag{4}$$

The central angle of the convex arc of the corrugated straight tube is halved to yield β . Applying the Law of Cosines and the complementary property of angles, β is determined as follows:

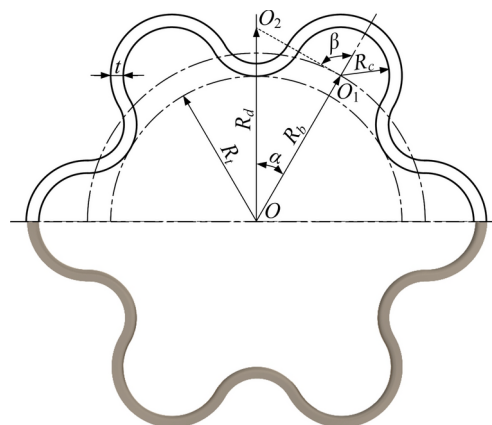


Fig. 2. Section size of the corrugated straight tube.

$$\beta = \pi - \cos^{-1} \left\{ \frac{\frac{1}{4}R_b - \sqrt{3R_c^2 - \frac{3}{16}R_b^2}}{2R_c} \right\} \quad (5)$$

The thickness of the corrugated straight tube is denoted as t . To ensure that the corrugated straight tube is a structurally reasonable design, the thickness t should satisfy the condition $0 < t < R_c$.

The size parameters of the convex guiding platform are illustrated in Fig. 3. The diameter of the upper end face of the frustum of a cone, denoted as D_1 , is determined based on the diameter of the inscribed circle of the corrugated straight tube. The diameter of the bottom end face of the frustum of a cone, denoted as D_2 , is determined based on the fully unfolded inner diameter of the convex and concave arcs of the corrugated straight tube. The diameter of the base of the convex guiding platform, denoted as D_3 , is determined based on the diameter of the guide straight tube installed with the energy absorption device. The height of the frustum of a cone is denoted as h_1 , and the height of the convex guiding platform is denoted as h_2 . Both h_1 and h_2 are determined by the displacement provided by the energy absorption mechanism. The curling radius of the convex guiding platform is denoted as R_0 , the width of the bottom platform of the convex guiding platform is denoted as a , the diameter of the screw threaded hole is denoted as D_4 , and the height of the screw threaded hole is denoted as h_3 .

Numerical simulation analysis of the energy absorption device

The corrugated straight tube flip-type energy absorption device is designed to work in conjunction with the ZQ4000/22/44 roadway unit support to enhance the impact resistance of the support system. The working resistance of a single column of the ZQ4000/22/44 roadway unit support is 2000 kN. To ensure that the energy absorption device does not buckle under quasi-static conditions and undergoes buckling deformation before the failure of the column under impact conditions, thereby achieving the effect of providing displacement and absorbing energy, the starting threshold of the energy absorption device is designed to be 1.2 to 1.5 times the working resistance of the column, i.e., 2400 kN to 3000 kN. With the size parameters of the guide sleeve of the column and the starting threshold of the energy absorption device as reference factors, the size parameters of the corrugated straight tube flip-type energy absorption device were preliminarily designed. The size parameters of the corrugated straight tube are as follows: the number of convex and concave arcs is 6 each, the base circle radius is 78 mm, the inner convex arc radius is 24 mm, the thickness is 6 mm, the height is 200 mm, and the inner fillet radius of the bottom end face is 3 mm. The size parameters of the convex guiding platform are as follows: the base diameter is 294 mm, the total height is 94 mm, the curling radius is 13.5 mm, the size of the screw threaded hole is M20 and the height of the threaded hole is 50 mm. The size parameters of the cover plate are as follows: the diameter is 289 mm, the thickness is 6 mm, and the through-hole diameter is 50 mm. Numerical simulations were conducted to analyze the buckling deformation process of the corrugated straight tube under axial impact conditions and to investigate the energy absorption and impact resistance characteristics of the energy absorption device.

Establishment of the simulation model

The three-dimensional model of the corrugated straight tube flip-type energy absorption device was constructed by SolidWorks 2023 and subsequently imported into finite element simulation software Abaqus 2020 to establish the simulation model. The convex guiding platform served as both the supporting structure and the flipping guiding mechanism for the energy absorption device. The material chosen for this component was 42CrMo, renowned for its high strength, excellent toughness, superior fatigue limit, and strong resistance to multiple impacts. The corrugated straight tube, serving as the primary energy absorption structure, required material properties that included high strength, high toughness, and high ductility. Accordingly, HG785D was selected as the material due to its compliance with these mechanical requirements. According to the Chinese national standard GB/T228.1–2021, “Tensile test of metallic materials—Part 1: Method of test at room temperature,” tensile tests were conducted on HG785D material samples using a universal testing machine. The stress–strain curve for HG785D material was obtained through these tensile tests and is presented in the Fig. 4. The material of the cover plate was Q235, which had good strength, plasticity and weldability. The physical and mechanical property parameters of each material were shown in Table 1.

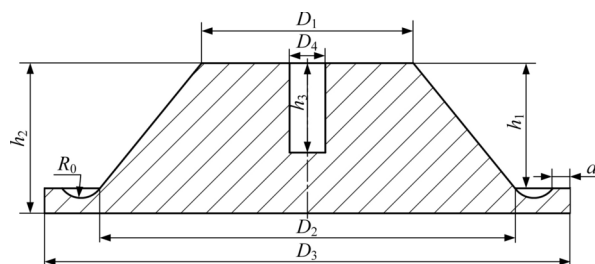


Fig. 3. Size parameters of the convex guiding platform.

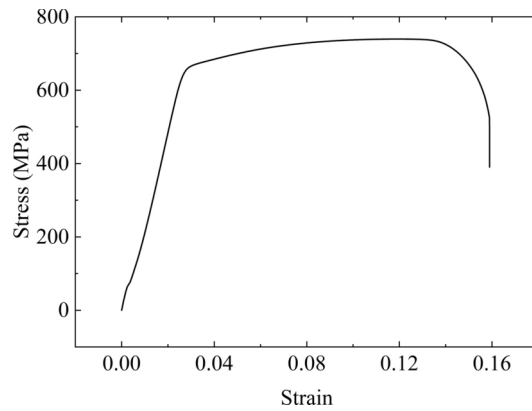


Fig. 4. Stress–strain curve of HG785D.

Material	Density ρ (kg/m ³)	Elastic modulus E (GPa)	Poisson's ratio μ	Yield strength σ_s (MPa)	Strength limit σ_b (MPa)
42CrMo	7850	212	0.280	930	1080
HG785D	7870	213	0.286	666	736
Q235	7830	210	0.274	235	380

Table 1. Physical and mechanical property parameters of materials.

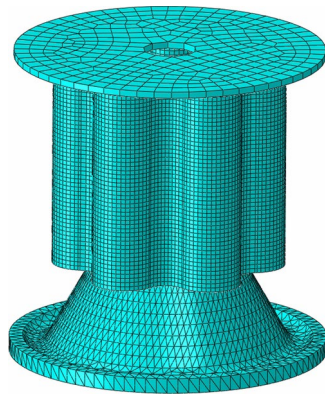


Fig. 5. Mesh model of energy absorption device.

To ensure the accuracy of the numerical simulation, the plastic properties of HG785D were considered, adopting the true yield strength and true strength limit to better reflect the actual physical characteristics of the material. Specifically, the true yield stress (σ_{st}) was set at 686 MPa, and the true strength limit (σ_{bt}) at 834 MPa.

For the contact type, a universal contact was employed. In the tangential direction, the “Penalty” friction mode was selected with a friction coefficient of 0.15. In the normal direction, the “Hard” contact mode was chosen. The convex guiding platform and the cover plate were treated as rigid bodies. The lower end face of the cover plate and the upper end face of the corrugated straight tube were constrained using the “Tie” constraint. The convex guiding platform was fully fixed. The crushing velocity was set to 4.5 m/s. The boundary condition for the cover plate was defined as displacement loading, with a loading value of 180 mm. The display dynamics analysis step time was set to 0.04 s. A quadratic hexahedral element, known for its high computational accuracy and efficiency, was utilized to mesh the corrugated straight tube. The mesh size was specified as 2 mm, with the number of mesh layers set to 4, resulting in a total of 19,364 elements. The model of energy absorption device after mesh division is shown in the Fig. 5.

Analysis of numerical simulation results

The buckling deformation process of the energy absorption device can be categorized into five distinct stages: the convex and concave arcs stretching stage, the end stretching and flaring stage, the end fitting stage, the curling deformation stage, and the rolling deformation stage. The corrugated straight tube moves vertically downward, and its bottom convex-concave arc is stretched by the lateral support of the convex guiding platform's circular table structure. Upon the bottom end of the corrugated barrel touching the curved rounded surface, the curved

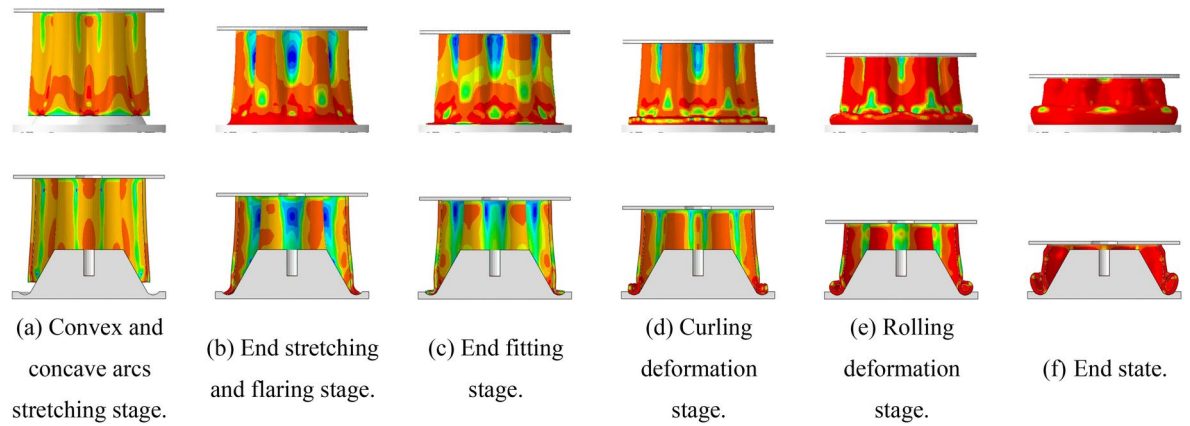


Fig. 6. The complete view and sectional view of the buckling deformation process of the energy absorption device.

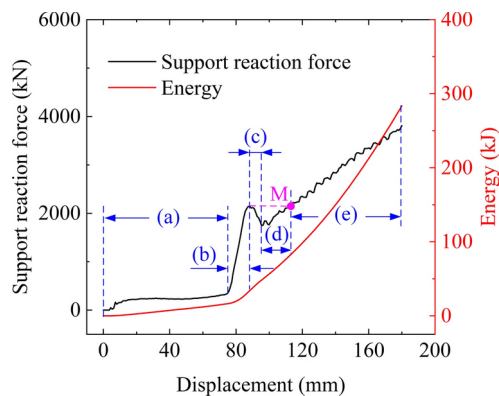


Fig. 7. Support reaction force–displacement curve and energy–displacement curve of the energy absorption device.

rounded surface guides the bottom end of the corrugated barrel to stretch and flare circumferentially. As the bottom end of the corrugated barrel reaches the lowest point of the rounded surface, the end of the corrugated barrel bends and deforms upward along the rounded surface due to the influence of the rounded surface structure. When the plastic bending moment of the material exceeds the counter-bending moment at the end, the end of the corrugated barrel rolls inward. This deformation process results in a flipping state of the corrugated straight tube. The complete view and sectional view of the buckling deformation process of the energy absorption device are depicted in Fig. 6. Additionally, the support reaction force–displacement curve and the energy–displacement curve of the energy absorption device during the buckling deformation process are illustrated in Fig. 7.

Figure 6a showed the convex and concave arcs stretching stage of the corrugated straight tube. When the corrugated straight tube moved vertically downward, the convex and concave arcs at the bottom of the corrugated straight tube gradually stretched due to the combined action of the axial compression load and the lateral support load of the convex guiding platform. When the bottom end of the corrugated straight tube moved to the initial position of the arc fillet surface, the convex and concave arcs of the bottom end were completely stretched into a circle. At this stage, the support reaction force of the energy absorption device increased slightly. When the convex and concave arcs were completely stretched into a circle, the support reaction force was 326.50 kN. Figure 6b showed the end stretching and flaring stage of the corrugated straight tube. The bottom end of the corrugated straight tube began to contact the arc fillet surface, and the circular diameter of the bottom end gradually increased. In this process, the corrugated straight tube bore axial compression load and circumferential stretching load. The support reaction force of the energy absorption device rose rapidly. When the bottom of the corrugated straight tube moved to the lowest point of the fillet surface, the support reaction force reached the initial peak value. The initial peak value of the support reaction force was 2148.32 kN. Figure 6c showed the end fitting stage of the corrugated straight tube. When the end of the corrugated straight tube moved to the lowest point of the fillet surface, it was guided by the fillet surface structure and gradually fitted the fillet surface. The bending deformation was the main deformation form of this process. The bending deformation caused the support reaction force of the energy absorption device to decline. When the bottom of the corrugated straight tube was separated from the fillet surface, the support reaction force reached the initial valley value. The initial valley value of the support reaction force was 1742.86 kN. Figure 6d showed the curling deformation stage. After

the end of the corrugated straight tube was separated from the fillet surface, the end of the corrugated straight tube curled upward due to the circumferential stretching load and the continuous axial compression load. The support reaction force increased with the increase of the compression displacement and then rose again to the initial peak value. Figure 6e showed the rolling deformation stage. When the plastic bending torque of the material was greater than the reverse bending torque of the end, the end of the corrugated straight tube rolled inward. Under the action of continuous axial compression load, the rolling part gradually formed a double-layer structure. At this stage, the support reaction force continued to rise. Finally, the support reaction force increased to 3813.07 kN. Figure 6f showed the end state of the corrugated straight tube flip-type energy absorption device.

The support reaction force–displacement curve and the energy–displacement curve of the energy absorption device during the buckling deformation process are illustrated in Fig. 7. The energy absorbed by the energy absorption device exhibited an overall upward trend, which can be primarily divided into two stages. In the first stage, due to the stretching of the convex and concave arcs at the bottom of the corrugated straight tube, and the stretching and flaring of the end of the corrugated straight tube, the energy increased gradually with the increase in compression displacement. In the second stage, as a result of the bending, curling, and rolling deformation of the end of the corrugated straight tube, the energy showed a rapid linear upward trend with the increase in compression displacement. The maximum energy absorbed in the test was 38.82 kJ, and the total energy absorbed by the energy absorption device during the buckling deformation process was 283.53 kJ.

Through the analysis of the numerical simulation results of the energy absorption device, it was observed that the support reaction force exhibited an overall upward trend during the axial crushing process, demonstrating its potential to provide effective support. The buckling deformation process absorbed a significant amount of energy, thereby fulfilling the dual functions of energy absorption and displacement provision. However, the initial peak value of the support reaction force in the preliminary design of the energy absorption device model did not meet the specified range. Consequently, by systematically analyzing the influence of key structural parameters on the device's response, the optimal structural parameters were determined.

Analysis of deformation energy absorption theory of the energy absorption device

The schematic diagrams of the flip-type deformation of the energy absorption device is illustrated in Fig. 8. Under the influence of an external axial load, the corrugated straight barrel moves downward. The bottom end of the corrugated straight barrel is supported by the round table surface, resulting in convex and concave arc stretching deformation. As the bottom end of the corrugated straight barrel moves from point A to point B, it is subjected to a circumferential tensile load, causing an increase in the circular diameter of the bottom end and resulting in tensile flapping deformation. The corrugated straight tube is guided by the curved rounded surface at point B, leading to bending and deformation. The bottom end of the corrugated straight tube subsequently moves from point B to point C and point D. Due to the plastic bending moment of the material exceeding the reverse bending moment at the end, the bottom end of the corrugated straight tube rolls and deforms inward after reaching point D. The radian of arc ABC has a certain influence on bending deformation of corrugated straight tubes. When the radian of arc ABC is large, the degree of stretching and flaring of the bottom end of the corrugated straight tube is large, and the bottom end of the corrugated straight tube has a better fitting with the arc fillet surface. So, the bending deformation of the corrugated straight tube is easier to achieve. As the radian of arc ABC decreases, the degree of stretching and flaring of the bottom end of the corrugated straight tube decreases, the degree of fitting between the bottom of the corrugated straight tube and the arc fillet surface becomes worse. The bending deformation of the corrugated straight tube is not easy to achieve. The initial radian of arc ABC is 2.11 rad.

The axial load during the buckling deformation process of the corrugated straight tube flip-type energy absorption device was analyzed using the energy method. Given that the frictional energy consumed in the deformation process has a negligible influence on the overall energy absorption effect compared to the energy absorption at each stage of deformation, its numerical value was temporarily disregarded. The deformation energy of the energy absorption device is primarily categorized into four types: convex arc stretching deformation energy, concave arc stretching deformation energy, stretching and flaring deformation energy, and bending deformation energy. Adhering to the principle of energy conservation, the work performed by the external axial

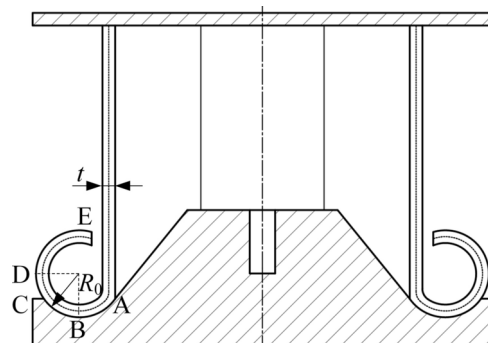


Fig. 8. The schematic diagrams of the flip-type deformation of the energy absorption device.

load is converted into these four types of deformation energy. This relationship can be mathematically expressed as follows:

$$dW_A = dW_{Et} + dW_{Ea} + dW_T + dW_F \quad (6)$$

where W_A represents the work done by the axial load, W_{Et} denotes the convex arc stretching deformation energy, W_{Ea} signifies the concave arc stretching deformation energy, W_T corresponds to the stretching and flaring deformation energy, and W_F indicates the bending deformation energy.

The material strengthening model is expressed as follows:

$$\bar{\sigma} = A\bar{\varepsilon}^n \quad (7)$$

where $\bar{\sigma}$ indicates the material equivalent stress, $\bar{\varepsilon}$ denotes the material equivalent strain, A signifies the material strengthening coefficient, n represents the material hardening index.

The volume remains unchanged during plastic deformation. Hence,

$$\varepsilon_r + \varepsilon_\theta + \varepsilon_t = 0 \quad (8)$$

where ε_r represents the longitudinal strain, ε_θ indicates the circumferential strain, ε_t signifies the thickness strain.

We assume that the thickness strain is zero. According to the equivalent strain calculation formula, the equivalent strain can be obtained as below:

$$\bar{\varepsilon} = \frac{2\sqrt{3}}{3}\varepsilon_\theta \quad (9)$$

The increment of stretching deformation energy for the convex arc can be expressed as:

$$dW_{Et} = \int_V \bar{\sigma}_{Et} d\bar{\varepsilon}_{Et} dV \quad (10)$$

where $\bar{\sigma}_{Et}$ is the equivalent stress of convex arc stretching deformation, $\bar{\varepsilon}_{Et}$ is the equivalent strain of the convex arc stretching deformation, V is the volume of the deformed portion of the corrugated straight tube.

The circumferential strain of convex arc stretching is expressed as:

$$\varepsilon_{\theta Et} = \frac{1}{2} \ln \left[\frac{(2R_c + t)(12\beta - \pi)}{24\beta R_c - 2\pi R_c + \pi t} \right] \quad (11)$$

By combining Eqs. (7), (9), (10) and (11), the increment of stretching deformation energy for the convex arc is obtained as :

$$dW_{Et} = \frac{6\beta t A (2R_c + t) dx}{n + 1} \left\{ \frac{\sqrt{3}}{3} \ln \left[\frac{(2R_c + t)(12\beta - \pi)}{24\beta R_c - 2\pi R_c + \pi t} \right] \right\}^{n+1} \quad (12)$$

The increment of stretching deformation energy for the concave arc can be expressed as:

$$dW_{Ea} = \int_V \bar{\sigma}_{Ea} d\bar{\varepsilon}_{Ea} dV \quad (13)$$

where $\bar{\sigma}_{Ea}$ is the equivalent stress of the concave arc stretching deformation, $\bar{\varepsilon}_{Ea}$ is the equivalent strain of the concave arc stretching deformation.

The circumferential strain for the concave arc stretching is expressed as:

$$\varepsilon_{\theta Ea} = \frac{1}{2} \ln \left[\frac{(2R_c - t)(12\beta R_c - \pi R_c + \pi t)}{R_c(24\beta R_c - 2\pi R_c + \pi t)} \right] \quad (14)$$

By combining Eqs. (7), (9), (13) and (14), the stretching deformation energy increment of concave arc is obtained as:

$$dW_{Ea} = \frac{tA(2R_c - t)(6\beta - \pi) dx}{n + 1} \left\{ \frac{\sqrt{3}}{3} \ln \left[\frac{(2R_c - t)(12\beta R_c - \pi R_c + \pi t)}{R_c(24\beta R_c - 2\pi R_c + \pi t)} \right] \right\}^{n+1} \quad (15)$$

The stretching and flaring deformation energy increment can be expressed as follow:

$$dW_T = \int_V \bar{\sigma}_T d\bar{\varepsilon}_T dV \quad (16)$$

where $\bar{\sigma}_T$ is the equivalent stress of circumferential stretching of corrugated straight tube, $\bar{\varepsilon}_T$ is the equivalent strain of circumferential stretching of corrugated straight tube.

The circumferential stretching strain of corrugated straight tube is expressed as:

$$\varepsilon_{\theta_T} = \ln \left[\frac{24\beta R_c - 2\pi R_c + 2\pi R_0 + \sqrt{\pi t(24\beta R_c - 2\pi R_c + 2\pi R_0)}}{24\beta R_c - 2\pi R_c + \pi t} \right] \quad (17)$$

By combining Eqs. (7), (9), (16) and (17), the stretching and flaring deformation energy increment is obtained as:

$$dW_T = \frac{tA(24\beta R_c - 2\pi R_c + \pi t) dx}{n + 1} \left\{ \frac{2\sqrt{3}}{3} \ln \left[\frac{24\beta R_c - 2\pi R_c + 2\pi R_0 + \sqrt{\pi t(24\beta R_c - 2\pi R_c + 2\pi R_0)}}{24\beta R_c - 2\pi R_c + \pi t} \right] \right\}^{n+1} \quad (18)$$

Upon contact between the bottom end of the corrugated straight tube and the convex guiding platform's curved rounded surface, the bottom end undergoes tensile flaring deformation. As the convex guiding platform's curling radius R_0 increases, the circumferential tensile strain of the corrugated straight tube increases, leading to a greater increment in tensile flaring deformation energy.

The bending deformation energy increment can be expressed as follow:

$$dW_C = \int_V \bar{\sigma}_C d\bar{\varepsilon}_C dV \quad (19)$$

where $\bar{\sigma}_C$ is the equivalent stress of bending deformation of corrugated straight tube, $\bar{\varepsilon}_C$ is the equivalent strain of bending deformation of corrugated straight tube.

The bending deformation strain of corrugated straight tube is expressed as:

$$\varepsilon_{\theta_C} = \ln \left[\frac{2\pi R_0 + \pi t + \sqrt{\pi t(24\beta R_c - 2\pi R_c + 2\pi R_0)}}{2\pi R_0 - \pi t + \sqrt{\pi t(24\beta R_c - 2\pi R_c + 2\pi R_0)}} \right] \quad (20)$$

By combining Eqs. (7), (9), (19) and (20), the bending deformation energy increment is obtained as:

$$dW_C = \frac{tA(24\beta R_c - 2\pi R_c + \pi t) dx}{n + 1} \left\{ \frac{2\sqrt{3}}{3} \ln \left[\frac{2\pi R_0 + \pi t + \sqrt{\pi t(24\beta R_c - 2\pi R_c + 2\pi R_0)}}{2\pi R_0 - \pi t + \sqrt{\pi t(24\beta R_c - 2\pi R_c + 2\pi R_0)}} \right] \right\}^{n+1} \quad (21)$$

Under the guiding effect of the rounded surface of the convex guiding platform, the bottom end of the corrugated straight tube experiences bending deformation. With an increase in the convex guiding platform's curling radius R_0 , the bending deformation strain of the corrugated straight tube decreases, resulting in a decrease in incremental bending deformation energy. Consequently, the corrugated straight tube's resistance to bending deformation diminishes, making the bending deformation of its end more easily achievable.

The increment of work done by axial load can be expressed as follow:

$$dW_A = F dx \quad (22)$$

where F is the external axial load, x is the length of the deformed part of the corrugated straight tube.

Substituting Eqs. (12), (15), (18), (21) and (22) into Eq. (6) and simplifying, the external axial load is obtained as:

$$\begin{aligned}
 F = & \frac{6\beta t A (2R_c + t)}{n + 1} \left\{ \frac{\sqrt{3}}{3} \ln \left[\frac{(2R_c + t)(12\beta - \pi)}{24\beta R_c - 2\pi R_c + \pi t} \right] \right\}^{n+1} \\
 & + \frac{t A (2R_c - t)(6\beta - \pi)}{n + 1} \left\{ \frac{\sqrt{3}}{3} \ln \left[\frac{(2R_c - t)(12\beta R_c - \pi R_c + \pi t)}{R_c (24\beta R_c - 2\pi R_c + \pi t)} \right] \right\}^{n+1} \\
 & + \frac{t A (24\beta R_c - 2\pi R_c + \pi t)}{n + 1} \left\{ \frac{2\sqrt{3}}{3} \ln \left[\frac{24\beta R_c - 2\pi R_c + 2\pi R_0 + \sqrt{\pi t (24\beta R_c - 2\pi R_c + 2\pi R_0)}}{24\beta R_c - 2\pi R_c + \pi t} \right] \right\}^{n+1} \quad (23) \\
 & + \frac{t A (24\beta R_c - 2\pi R_c + \pi t)}{n + 1} \left\{ \frac{2\sqrt{3}}{3} \ln \left[\frac{2\pi R_0 + \pi t + \sqrt{\pi t (24\beta R_c - 2\pi R_c + 2\pi R_0)}}{2\pi R_0 - \pi t + \sqrt{\pi t (24\beta R_c - 2\pi R_c + 2\pi R_0)}} \right] \right\}^{n+1}
 \end{aligned}$$

The following parameters were used in the numerical simulation: basic circle radius $R_b = 78$ mm, inner convex arc radius $R_c = 24$ mm, thickness $t = 6$ mm, curling radius $R_0 = 13.5$ mm, material strengthening coefficient $A = 1450$ MPa, and material hardening index $n = 0.2$. These values were substituted into Eq. (23). When the bending deformation of the energy absorption device reached a stable state, the applied external axial load was 2039.15 kN. As shown in Fig. 7, at the conclusion of the curling deformation phase of the energy absorption device, the support reaction increased again to the initial peak value and then entered a stage of stable rolling bending deformation. During this stage, the end of the corrugated straight tube formed a double-layer structure, and the support reaction increased steadily. Based on the numerical simulation results, the support reaction of the energy absorption device in a stable state of bending deformation was 2148.32 kN (Point M in Fig. 7). The applied external axial load (2039.15 kN) when the bending deformation of the energy absorption device reaches a stable state obtained by theoretical analysis is compared with the support reaction force (2148.32 kN) obtained by numerical simulation when the energy absorption device is in a stable state of bending deformation. The error rate between the two was 5.08%, thereby validating the accuracy of the theoretical model.

Through the analysis of Eqs. (5) and (23), it is determined that, given a specific material for the energy absorption device, the external axial load is influenced by four primary structural parameters: the basic circle radius (R_b), the inner convex arc radius (R_c), the thickness (t) of the corrugated straight tube, and the curling radius (R_0) of the convex guiding platform. Consequently, these four main structural parameters exert a significant influence on the energy absorption characteristics of the energy absorption device.

Response characteristics analysis and structural parameters optimization of the energy absorption device

The response surface design method involves the rational design of test groups based on input influencing factors. After the test, the corresponding response values of each test group are input for subsequent analysis. This method employs a multiple quadratic regression equation as the regression analysis mathematical model to describe the functional relationship between the influencing factors and the response values. Additionally, it facilitates the analysis of interactions between influencing factors. By utilizing statistical analysis methods, the optimal combination of influencing factors can be determined based on the regression equation and the desired target response effect^{40–43}. In this study, the Central Composite Circumscribed design method (CCC), which possesses both sequential and rotational properties and offers high prediction accuracy, is chosen to analyze the response characteristics of the energy absorption device and to optimize the structural parameters of the corrugated straight tube.

Response surface test design, results and residual analysis

Based on the main structural parameters affecting the energy absorption characteristics of the device, as discussed in Chapter 4, four key structural parameters were selected as independent variables: the basic circle radius (R_b), the inner convex arc radius (R_c), the thickness (t) of the corrugated straight tube, and the curling radius (R_0) of the convex guiding platform. Three response values were chosen as dependent variables: the initial peak value of the support reaction force (F_{cmax}), the average support reaction force (F_m) within the 70 mm to 180 mm compression displacement range, and the total energy (E_z) absorbed by the device. The CCC module in Design-Expert 13 was utilized to design a four-factor, five-level test scheme, resulting in a total of 30 experimental combinations. The structural parameters and their levels are presented in Table 2, while the test schemes and corresponding response values for each group are detailed in Table 3.

Based on the data in Table 3, the values of the fitting coefficient (R^2), the adjusted fitting coefficient (Adjusted R^2), and the predicted fitting coefficient (Predicted R^2) were calculated for different prediction models of each

Influencing factor	Level				
	-2	-1	0	1	2
R_b (mm)	76	78	80	82	84
R_c (mm)	21	22	23	24	25
t (mm)	5.5	6.0	6.5	7.0	7.5
R_0 (mm)	12.0	12.5	13.0	13.5	14.0

Table 2. Structural parameters and levels.

Std	Run	Influencing factor				Response value		
		R_b (mm)	R_c (mm)	t (mm)	R_0 (mm)	F_{cmax} (kN)	F_m (kN)	E_z (kJ)
23	1	80	23	6.5	12.0	3265.10	3453.04	400.61
13	2	78	22	7.0	13.5	3263.04	3518.95	411.14
22	3	80	23	7.5	13.0	4707.66	4507.26	520.99
2	4	82	22	6.0	12.5	2777.73	2891.88	342.65
18	5	84	23	6.5	13.0	3217.93	3138.88	372.41
7	6	78	24	7.0	12.5	3460.46	3711.20	425.86
16	7	82	24	7.0	13.5	3271.76	3574.46	416.11
28	8	80	23	6.5	13.0	2882.44	3170.92	369.79
24	9	80	23	6.5	14.0	2661.37	2898.50	339.74
26	10	80	23	6.5	13.0	2882.44	3170.92	369.79
10	11	82	22	6.0	13.5	2526.71	2659.04	317.02
27	12	80	23	6.5	13.0	2882.44	3170.92	369.79
3	13	78	24	6.0	12.5	2413.52	2732.83	315.50
8	14	82	24	7.0	12.5	3554.16	3806.22	441.54
19	15	80	21	6.5	13.0	3484.08	3296.90	392.46
21	16	80	23	5.5	13.0	1862.26	2192.50	257.22
11	17	78	24	6.0	13.5	2148.32	2443.79	283.53
12	18	82	24	6.0	13.5	2229.70	2553.84	298.88
14	19	82	22	7.0	13.5	4182.36	4047.33	475.92
4	20	82	24	6.0	12.5	2462.07	2854.34	332.04
5	21	78	22	7.0	12.5	3667.71	3861.68	448.61
25	22	80	23	6.5	13.0	2882.44	3170.92	369.79
30	23	80	23	6.5	13.0	2882.44	3170.92	369.79
20	24	80	25	6.5	13.0	2792.36	3067.97	354.80
1	25	78	22	6.0	12.5	2449.30	2758.82	322.44
17	26	76	23	6.5	13.0	2788.24	3039.75	351.52
9	27	78	22	6.0	13.5	2216.56	2487.57	292.57
15	28	78	24	7.0	13.5	3145.07	3404.32	393.77
6	29	82	22	7.0	12.5	4279.63	4015.35	472.33
29	30	80	23	6.5	13.0	2882.44	3170.92	369.79

Table 3. Design scheme and results of response surface test.

response value. The analysis indicated that the prediction models for F_{cmax} and E_z were quadratic, while the prediction model for F_m was a two-factor interaction (2FI) model. Residual analysis was conducted based on these prediction models. Figures 9, 10, 11 present the normal probability plots of the internally studentized residuals, the plots of the internally studentized residuals versus the predicted values, and the plots of the predicted values versus the actual values for each response value.

The distribution of test points for each response value was relatively balanced, and the residuals exhibited a near-linear normal probability plot, indicating a good correlation for the prediction models. The internally studentized residuals and predicted values for each response value were randomly distributed around zero without any discernible pattern, suggesting good reliability of the prediction models. Additionally, the predicted values aligned well with the actual values for each response, closely following the fitted line without significant deviations, which further attests to the good fit of the prediction models.

Test the significance of structural parameters based on analysis of variance

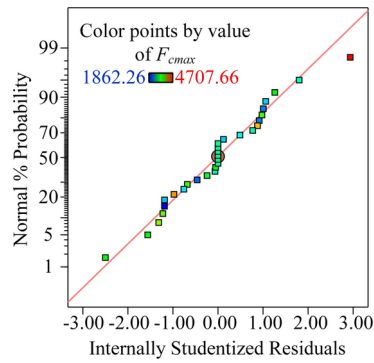
Significance analysis of the F_{cmax}

Based on the Quadratic model, the prediction model for the F_{cmax} was developed, and the fitting statistical data are presented in Table 4. Analysis revealed that the prediction model for the F_{cmax} meets the specified requirements.

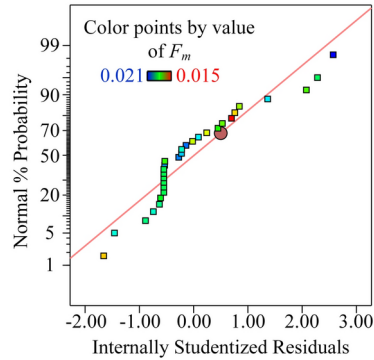
The multiple regression equation for F_{cmax} , influenced by the variables R_b , R_c , t , and R_0 , is presented in Eq. 24.

$$\begin{aligned}
 F_{cmax} = & -17064.67292 + 113.06604R_b + 3350.98292R_c - 4093.21583t - 2006.01583R_0 \\
 & - 56.85937R_bR_c + 61.44500R_bt + 22.18375R_bR_0 - 155.57500R_ct - 13.70750R_cR_0 \\
 & - 29.60000R_0t + 3.60828R_b^2 + 48.21688R_c^2 + 339.60750t^2 + 17.88250R_0^2
 \end{aligned} \quad (24)$$

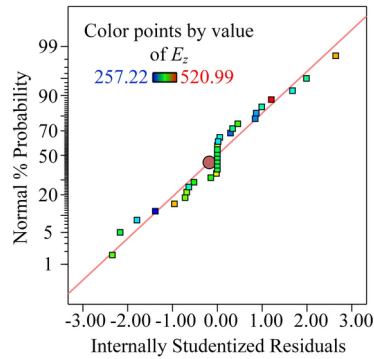
Variance analysis was performed based on the regression equation of the prediction model. The F-value of the F_{cmax} prediction model was 68.76, and the P-value was less than 0.0001, indicating that the model was significant



(a) Initial peak value of the support reaction force.



(b) Everage support reaction force.



(c) Total energy.

Fig. 9. Normal distribution probability diagrams of the internally studentized residuals.

and could better fit the test results. The P-values for R_b , R_c , t , and R_0 , the interaction terms $R_b R_c$, $R_b t$, and $R_c t$, and the quadratic terms R_c^2 and t^2 were all less than 0.05, indicating that these factors had a significant effect on F_{cmax} .

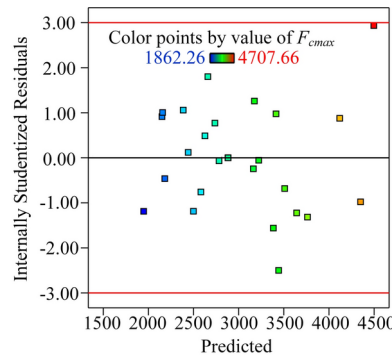
The F-values of each structural parameter were analyzed as follows: $F_t(783.64) > F_{R_c}(55.28) > F_{R_b}(38.28) > F_{R_0}(36.24)$. The analysis showed that the thickness (t) had the greatest influence on the initial peak of the reaction force, followed by the inner convex arc radius (R_c) and the basic circle radius (R_b), while the curling radius (R_0) had the least influence on the initial peak value of the support reaction force.

Significance analysis of the F_m

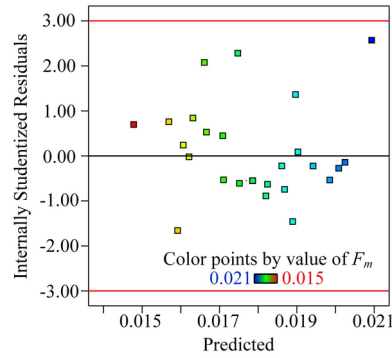
According to the 2FI model for the F_m , the fitting statistical data are presented in Table 5. After analysis, it was found that the average branch reaction prediction model meets the specified requirements.

The multiple regression equation for F_m , influenced by R_b , R_c , t and R_0 , is shown in Eq. 25.

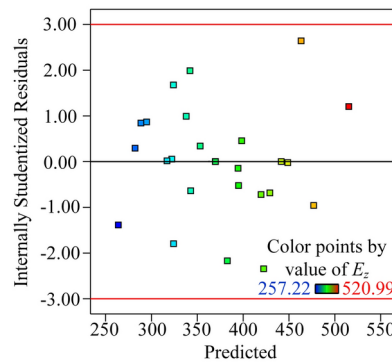
$$F_m^{-0.5} = 0.021096 + 0.000214R_b - 0.005007R_c + 0.000513t + 0.007860R_0 + 0.000034R_b R_c - 7.26253 \times 10^{-6} R_b t - 0.000080R_b R_0 + 0.000157R_c t + 0.000113R_c R_0 - 0.000509R_0 t \tag{25}$$



(a) Initial peak value of the support reaction force.



(b) Average support reaction force.



(c) Total energy.

Fig. 10. Distribution diagrams of the internally studentized residuals and the predicted values.

Variance analysis was conducted using the regression equation of the F_m prediction model. The F-value of the F_m prediction model was 185.44, with a P-value less than 0.0001, indicating that the model was statistically significant and exhibited a good fit to the experimental results. The P-values for R_b , R_c , t , R_0 , and the interaction term R_0t were all below 0.05, confirming that these factors had a significant influence on F_m .

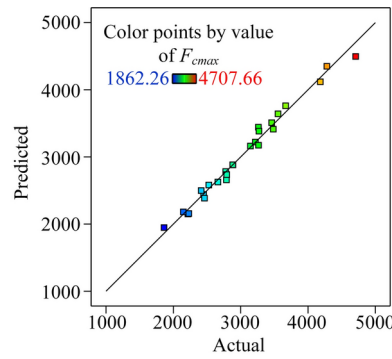
The F-values for each structural parameter were analyzed as follows: $F_t(1688.88) > F_{R_0}(101.14) > F_{R_b}(26.20) > F_{R_c}(20.85)$. This analysis revealed that the degree of influence of each structural parameter on the average support reaction force was ranked as follows, from greatest to least: thickness (t), curling radius (R_0), basic circle radius (R_b), and inner convex arc radius (R_c).

Significance analysis of the E_z

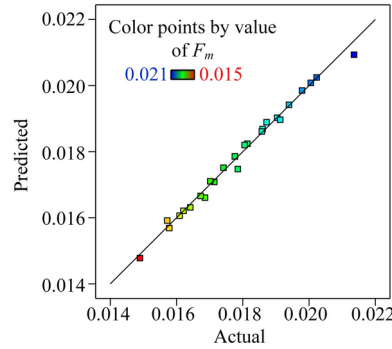
Using the Quadratic model for the E_z , the fitting statistical data are presented in Table 6. After analysis, it was determined that the total energy absorption prediction model meets the required criteria.

The multiple regression equation for E_z , influenced by R_b , R_c , t and R_0 , is shown in Eq. 26.

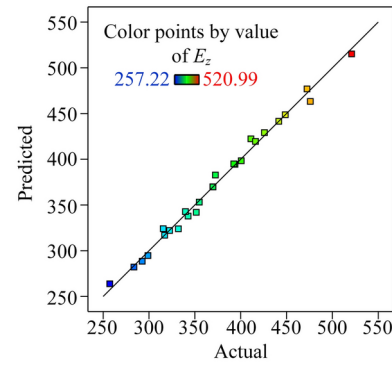
$$\begin{aligned}
 E_z = & -2617.58792 + 62.92354R_b + 222.45875R_c - 228.67750t - 254.79917R_0 \\
 & - 1.97656R_bR_c + 3.12313R_bt + 3.17313R_bR_0 - 10.74875R_ct - 4.15875R_cR_0 \\
 & + 7.30750R_0t - 0.461953R_b^2 + 1.06844R_c^2 + 19.74875t^2 + 0.818750R_0^2
 \end{aligned}
 \tag{26}$$



(a) Initial peak value of the support reaction force.



(b) Everage support reaction force.



(c) Total energy.

Fig. 11. Distribution diagrams of the predicted values and the actual values.

Name	Numerical value	Data good feature
R ²	0.9847	The value is close to 1, and the difference between Adjusted R ² and Predicted R ² is less than 0.2
Adjusted R ²	0.9703	
Predicted R ²	0.9116	
Coefficient of variation C.V	3.71%	Small value
Ratio of signal to noise Adeq Precision	32.3241	Values greater than 4

Table 4. Statistical fitting of the prediction model of the F_{cmax} .

Variance analysis was performed based on the regression equation of this prediction model. The F-value for the E_z prediction model was 138.20, with a P-value less than 0.0001, indicating that the model was statistically significant and provided a good fit to the test results. The P-values for R_b , R_c , t , R_0 , the interaction term $R_c t$, and the quadratic term t^2 were all below 0.05, confirming that these factors had a significant effect on E_z .

Name	Numerical value	Data good feature
R ²	0.9899	The value is close to 1, and the difference between Adjusted R ² and Predicted R ² is less than 0.2
Adjusted R ²	0.9845	
Predicted R ²	0.9721	
Coefficient of variation C.V	1.03%	Small value
Ratio of signal to noise Adeq Precision	55.4138	Values greater than 4

Table 5. Statistical fitting of the prediction model of the F_m .

Name	Numerical value	Data good feature
R ²	0.9923	The value is close to 1, and the difference between Adjusted R ² and Predicted R ² is less than 0.2
Adjusted R ²	0.9851	
Predicted R ²	0.9557	
Coefficient of variation C.V	1.99%	Small value
Ratio of signal to noise Adeq Precision	47.9009	Values greater than 4

Table 6. Statistical fitting of the prediction model of the E_z .

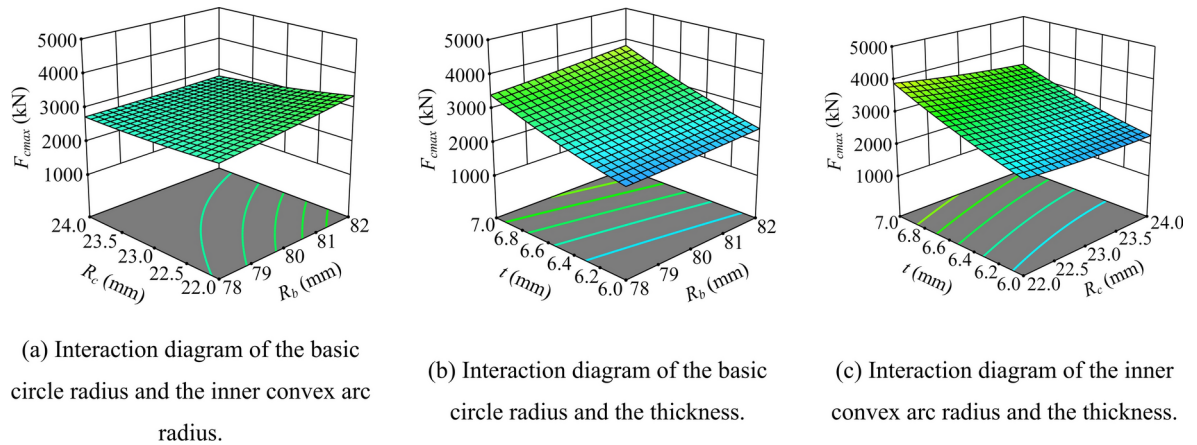


Fig. 12. Interaction diagrams of the significant interaction terms on the initial peak value of the support reaction force.

The F-values for each structural parameter were analyzed as follows: $F_t(1720.87) > F_{R_0}(84.28) > F_{R_c}(47.58) > F_{R_b}(45.36)$. This analysis revealed that the thickness (t) had the greatest influence on total energy absorption, followed by the curling radius (R_0). The influence of the inner convex arc radius (R_c) and the basic circle radius (R_b) on total energy was similar, with the inner convex arc radius having a slightly greater impact than the basic circle radius.

Interaction analysis of structural parameters on response values

Initial peak value of the support reaction force

The initial peak value of the support reaction force serves as a critical evaluation index for the energy absorption characteristics of the energy absorption device. Figure 12 illustrates the interaction diagrams of the structural parameters with significant effects on the initial peak value of the support reaction force.

As shown in Fig. 12a, when the thickness is 6.5 mm and the curling radius is 13 mm, the basic circle radius and the inner convex arc radius interact significantly on the initial peak of the support reaction force. When R_b increases from 78 to 82 mm, R_c values of 22 mm and 24 mm correspond to F_{cmax} ranges of 2859.78 kN to 3364.44 kN and 2748.67 kN to 2804.08 kN, respectively. When the R_c value is smaller, the variation in F_{cmax} is more pronounced. This is because, with a smaller R_c value, the cross-sectional area changes more significantly after the bottom of the corrugated straight tube is fully stretched, leading to more substantial changes in the bending force arm at the bottom of the corrugated straight tube. Consequently, the corrugated straight tube's resistance to bending deformation increases, resulting in more significant variations in F_{cmax} . The Fig. 13. is shown as a picture of the change of the bending force arm of the energy absorption device corresponding to the R_c values of 22 mm and 24 mm, respectively.

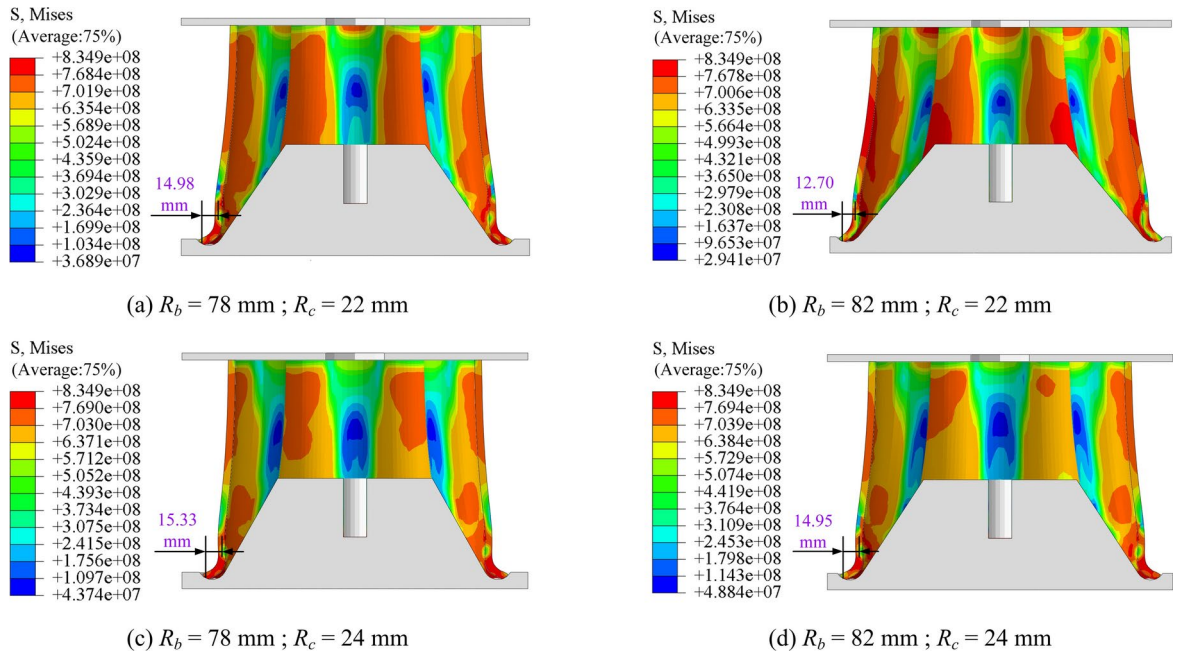


Fig. 13. $R_c = 22$ mm and $R_c = 24$ mm corresponding to the energy absorption device bending force arm changes.

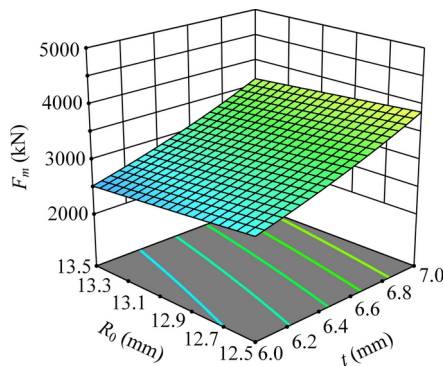


Fig. 14. Interaction diagram of the curling radius and the thickness on the average support reaction force.

As illustrated in Fig. 12b and c, when $R_b = 80$ mm, $R_c = 23$ mm, and $R_0 = 13$ mm, the variation range of F_{cmax} corresponding to an increase in t from 6 to 7 mm is from 2331.67 kN to 3601.79 kN, indicating that F_{cmax} is positively correlated with t . This positive correlation arises because, with the increase in t , the cross-sectional area of the bottom end of the corrugated straight tube involved in bending deformation exhibits a noticeable upward trend. Consequently, the resistance of the corrugated straight tube to bending deformation is enhanced. Furthermore, when $R_b = 80$ mm, $t = 6.5$ mm, and $R_0 = 13$ mm, a decrease in R_c from 24 to 22 mm corresponds to a variation range of F_{cmax} from 2762.85 kN to 3100.42 kN. In this scenario, F_{cmax} exhibits a linear upward trend as R_c decreases.

Average support reaction force

The average support reaction force reflects the overall load-bearing capability of the energy absorption device. The interaction effect of the significant interaction term $R_0 t$ on the average support reaction force within the 70 mm to 180 mm compression displacement range is illustrated in Fig. 14.

When $R_b = 80$ mm, $R_c = 23$ mm, and $t = 6.5$ mm, the dimensions of the corrugated straight tube remain constant. Changing R_0 from 12.5 to 13.5 mm results in a decrease in the F_m value from 3273.63 to 3013.08 kN, indicating a downward trend in the average support reaction force. This trend is attributed to the increase in R_0 , which deepens the curved rounded surface and enhances the degree of stretching and flaring at the lowest point of the corrugated straight tube’s rounded surface. Consequently, the bending force arm at the bottom of the corrugated straight tube increases, weakening its ability to resist bending deformation. This makes the subsequent bonding, curling, and rolling deformation processes at the corrugated straight tube’s end easier

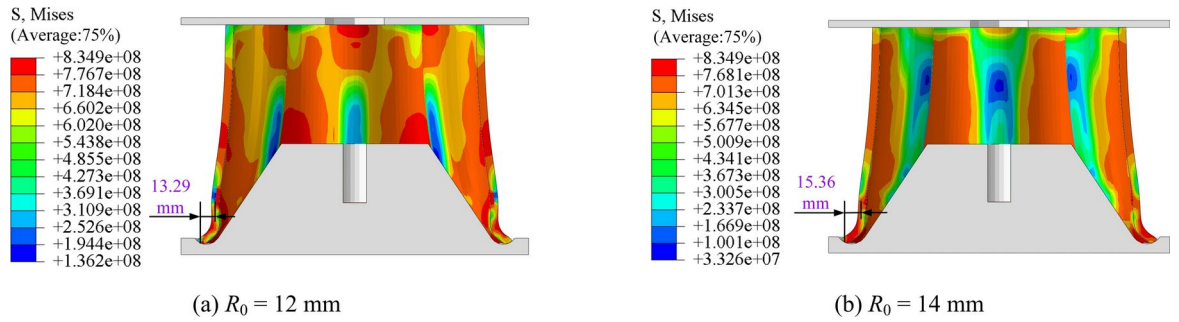


Fig. 15. $R_0 = 12$ mm and $R_0 = 14$ mm corresponding to the energy absorption device bending force arm changes.

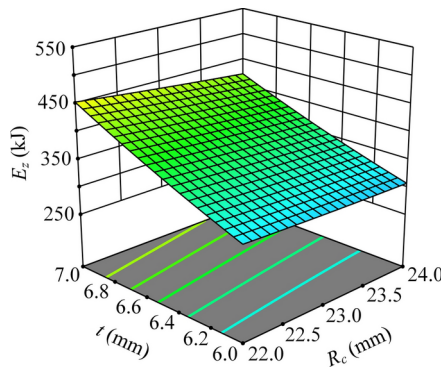


Fig. 16. Interaction diagram of the inner convex arc radius and the thickness on the total energy.

to achieve, thereby reducing the overall load-bearing capacity of the energy absorption device. The Fig. 15. is shown as a picture of the change of the bending force arm of the energy absorption device corresponding to the R_0 values of 12.5 mm and 13.5 mm, respectively.

Compared to R_0 , the influence of t on F_m is more significant. The volume of the corrugated straight tube involved in buckling deformation and the load-bearing capacity of the energy absorption device are positively correlated with t . The maximum value of F_m occurs when t is at its maximum ($t = 7$ mm) and R_0 is at its minimum ($R_0 = 12.5$ mm).

Total energy

The total energy refers to the sum of energy absorption in the buckling deformation process of the energy absorption device, and its value reflects the energy absorption effect of the energy absorption device. When the basic circle radius was 80 mm and the curling radius was 13 mm, the interaction response effect of the inner convex arc radius and the thickness on the total energy was shown in Fig. 16.

When $R_b = 80$ mm, $t = 6.5$ mm and $R_0 = 13$ mm, R_c decreases from 24 to 22 mm, E_z varies from 360.51 kJ to 381.93 kJ. When $R_b = 80$ mm, $R_c = 23$ mm and $R_0 = 13$ mm, E_z varies from 311.95 kJ to 437.55 kJ as t increases from 6 to 7 mm. Compared with the effect of R_c on E_z , t has a greater effect on the cross section area, which in turn has a more significant effect on E_z . When R_c is the smallest ($R_c = 22$ mm) and t is the largest ($t = 7$ mm), E_z is the largest.

Acquisition of optimal structural parameters of the energy absorption device

In the specified value ranges for the basic circle radius, inner convex arc radius, thickness, and curling radius, a higher initial peak value of the support reaction force within the range of 2400–3000 kN, along with a higher average support reaction force and total energy, indicated better energy absorption and impact resistance of the energy absorption device. Using Design-Expert 13 software, each structural parameter was optimized and analyzed based on multiple regression equations and response value optimization objectives. This process yielded five groups of optimization test schemes, as detailed in Table 7. According to the optimization objectives, the response values of the five groups of schemes were compared, and the fifth group was selected as the optimal scheme. The optimal structural parameters were as follows: the basic circle radius was 80.285 mm, the inner convex arc radius was 22.881 mm, the thickness was 6.555 mm, and the curling radius was 12.993 mm.

Considering the practical aspects of manufacturing the energy absorption device, the optimal structural parameters needed to be rounded. After rounding, the structural parameters were as follows: the basic circle radius was 80 mm, the inner convex arc radius was 23 mm, the thickness was 6.5 mm, and the curling radius was 13 mm. Numerical simulation analysis of the energy absorption device was then conducted based on these

Number	R_b (mm)	R_c (mm)	t (mm)	R_0 (mm)	F_{cmax} (kN)	F_m (kN)	E_z (kJ)
1	81.907	22.089	6.344	13.445	2999.913	3012.582	361.758
2	81.651	22.141	6.253	12.638	2999.393	3065.427	363.825
3	80.262	22.135	6.427	12.980	2999.995	3123.060	372.109
4	81.954	22.057	6.215	12.673	2999.779	3032.669	360.181
5	80.285	22.881	6.555	12.993	3000.000	3216.609	379.757

Table 7. Optimization test schemes.



Fig. 17. Corrugated arc pressing machine.

rounded size parameters. The numerical simulation results were compared with those of the optimal test scheme. The initial peak value error rate was 3.92%, the average support reaction force error rate was 1.42%, and the total energy error rate was 2.62%, all of which were less than 5%. The energy absorption device designed based on the rounded structural parameters demonstrated excellent energy absorption and impact resistance performance.

Numerical simulation and impact test of energy absorption device with optimal structural parameters

Numerical simulation analysis of energy absorption device with optimal structural parameters

The three-dimensional model of the corrugated straight tube flip-type energy absorption device is constructed using the optimized structural dimension parameters. This model is subsequently subjected to numerical simulation. Reflecting the actual downhole application scenario, the device is first preloaded, and the preloaded model is then simulated and analyzed. The simulation parameters are consistent with those specified in Section "Establishment of the simulation model". The loading mode for the energy absorption device is concentrated force loading. A static load of 400 kN is applied to the device, followed by an impact load of 4500 kN. The numerical simulation results are compared with the impact test results to validate the model's accuracy and effectiveness.

Impact test research on optimal structural parameters of energy absorption device

The processing materials for the corrugated straight tube, cover plate, and convex guiding platform were HG785D, Q235 mold steel, and 42CrMo mold steel, respectively. The energy absorption device was fabricated according to the optimal structural size parameters after rounding. The cover plate and convex guiding platform were processed using cutting and turning processes. Considering the processing size, structure, and cost of the corrugated straight tube, it was formed using a corrugated arc pressing machine, as depicted in Fig. 17. The bottom end of the corrugated straight tube was rounded, and the corrugated straight tube and cover plate were fixed via welding. The final processed energy absorption device is shown in Fig. 18.

In this experiment, dynamic impact testing was conducted using a 6500 kN hydraulic impact testing machine. This machine is capable of delivering a maximum impact force of 6500 kN, with a maximum impact energy of 4.4×10^6 J and a maximum impact velocity of 8 m/s, over an impact stroke of 0.8 m. To monitor the performance of the energy absorption device during impact, a TST5912 multi-channel dynamic signal acquisition system was employed to record support reaction forces and displacements. Additionally, the impact process was captured using a high-speed camera. To facilitate dynamic impact testing on the energy absorption device, the pre-pressed device was placed within a box. Following the application of a static load of 400 kN, a dynamic impact load of 4500 kN was applied. The overall test setup is illustrated in Fig. 19.



Fig. 18. General assembly drawing of the corrugated straight tube flip-type energy absorption device.

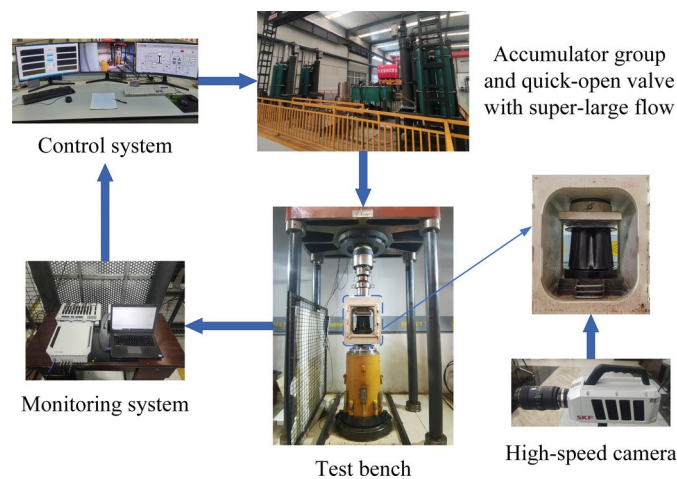


Fig. 19. Impact test system.

Comparative analysis of numerical simulation and impact test

Figure 20. illustrates the buckling deformation process of the energy absorption device under impact load, as captured by both numerical simulation and a high-speed camera. During the pre-pressed process, the convex and concave arcs completed their stretching. Consequently, the buckling deformation process can be divided into four distinct stages: the end stretching and flaring stage, the end fitting stage, the curling deformation stage, and the rolling deformation stage. The deformation states observed in each stage were generally consistent with the results of the numerical simulation.

Under the simulation and test conditions for the energy absorption device, Fig. 21. presents the branch-reaction and energy-displacement curves of the device. The support reaction's change trend can be divided into five distinct stages:

- **Slow Rise Stage:** The support reaction increases gradually as the convex and concave arcs at the bottom stretch. Upon complete stretching into a circle, the simulated support reaction reaches 429.65 kN, while the test support reaction is 391.50 kN.
- **Rapid Rise Stage:** The support reaction increases sharply when the bottom of the corrugated straight tube moves to the bottom of the rounded surface. The initial peak for the simulated support reaction is 2882.44 kN, and for the test, it is 2710.91 kN.
- **Decline Stage:** As the end of the corrugated straight tube separates from the rounded surface, the support reaction drops to an initial valley value. The simulated support reaction's initial valley value is 1987.26 kN, and the test value is 1838.12 kN.
- **Second Rise to Initial Peak:** In this stage, the bottom of the corrugated straight tube curls upward, and with increasing compression displacement, the support reaction rises again to the initial peak value.
- **Continuous Rise Stage:** The bottom end of the corrugated straight tube rolls inward and deforms, causing the support reaction to continue rising. The final simulated support reaction is 4760.59 kN, and the test support reaction reaches 4539.08 kN.

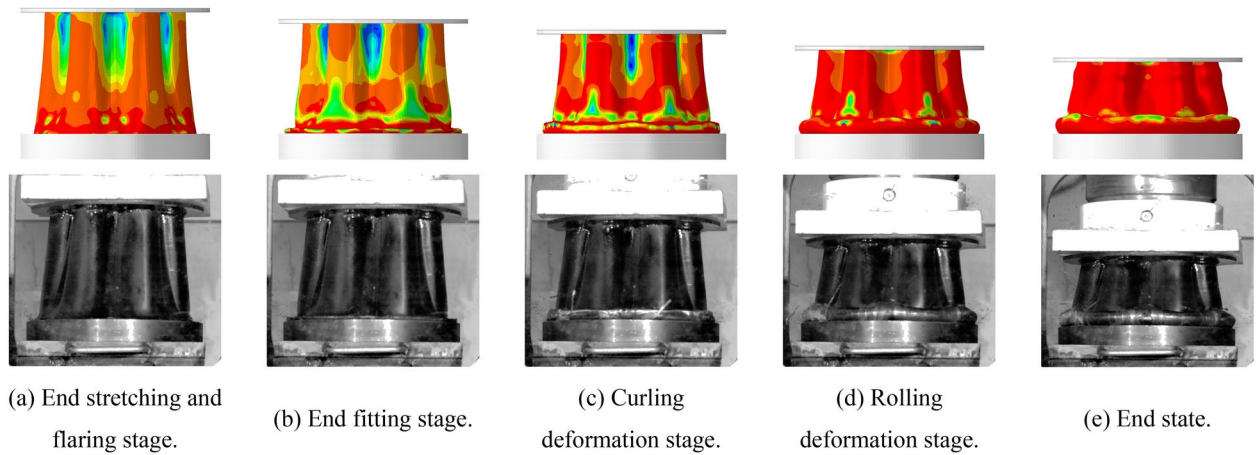


Fig. 20. Comparison of deformation process between numerical simulation and impact test of energy absorption device.

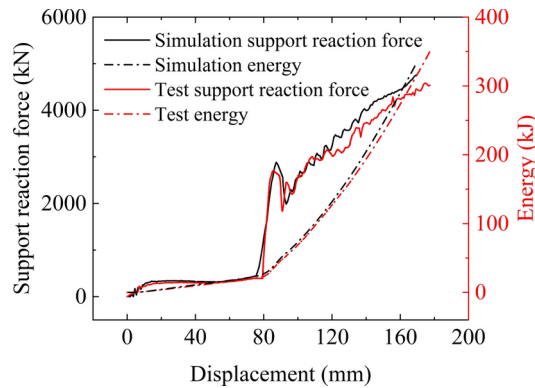


Fig. 21. Numerical simulation and impact test of energy absorption device support reaction force, energy absorption and displacement curves.

	First stage final support reaction force (kN)	F_{cmax} (kN)	Initial valley value of support reaction force (kN)	Final support reaction force (kN)	F_m (kN)	E_c (kJ)
Simulation	429.65	2882.44	1987.26	4760.59	3263.74	334.15
Test	391.50	2710.91	1838.12	4539.08	3028.10	349.89
Error rate	9.74%	6.33%	8.11%	4.88%	7.78%	4.50%

Table 8. Error analysis table of numerical simulation and test results.

Furthermore, the average support reaction during the main deformation process of the energy absorption device is 3263.74 kN in simulation and 3028.10 kN in the test.

As the compression displacement increases, the corrugated straight tube absorbs energy during each stage of deformation, with the absorbed energy exhibiting an upward trend. The maximum absorbed energy in the simulation is 334.15 kJ, while the test results show a maximum absorbed energy of 349.89 kJ. A comparison of the numerical simulation and impact test results is presented in Table 8, revealing that the error rate between the simulation and test data is less than 10%. This indicates a high level of consistency between the simulation and experimental results.

By analyzing the buckling deformation process of the energy absorption device under both numerical simulation and impact loading, as well as the variation trends of support reaction and energy absorption, it was found that within the range of impact displacement, the initial threshold was within 1.2 to 1.5 times the working resistance. The average support reaction force of the energy absorption device with optimal dimensions was higher. The rising trend in the support reaction force in the later stages was capable of supporting the weight of the collapsed rock mass following a rock burst, thereby preventing secondary damage to the column. The total

energy absorbed by the device achieved the desired energy absorption and anti-impact effects on the column. The optimized energy absorption device thus met the design requirements.

Conclusion

1. A novel corrugated straight tube flip-type energy absorption device was designed and investigated for application in roadway anti-impact hydraulic support systems. Numerical simulation results demonstrated that the buckling deformation process of this energy absorption device effectively achieved both energy dissipation and displacement provision functions.
2. The corrugated straight tube flip-type energy absorption device exhibited superior performance characteristics, particularly in maintaining a higher average support reaction force. This feature ensured continuous support functionality of the hydraulic system during the energy absorption process. The progressive upward trend of the support reaction force in the later stages effectively mitigated secondary damage to the column caused by rock mass collapse. Furthermore, the linear upward trend in energy absorption indicated excellent energy dissipation and anti-impact performance of the device.
3. Parametric analysis revealed that the thickness of the corrugated straight tube exerted the most significant influence on three critical performance indicators: the initial peak support reaction force, average support reaction force, and total energy absorption capacity. These parameters exhibited positive correlations with tube thickness. Additionally, the average support reaction force increased with decreasing curling radius of the convex guiding platform. The inner convex arc radius demonstrated negative correlations with both the initial peak support reaction force and total energy absorption. Moreover, the basic circle radius showed a positive correlation with the initial peak support reaction force.
4. Through comprehensive optimization analysis, the optimal structural parameters for the energy absorption device were determined as follows: base circle radius of 80 mm, inner convex arc radius of 23 mm, thickness of 6.5 mm, and curling radius of 13 mm. Dynamic impact testing and numerical simulation of the optimized device confirmed its superior energy absorption and anti-impact characteristics, validating the effectiveness of the design optimization process.

Data availability

The data that support the findings of this study are available on request from the corresponding author, upon reasonable request.

Received: 29 October 2024; Accepted: 12 February 2025

Published online: 19 February 2025

References

1. Qi, Q. X. et al. Theory and technical framework of coal mine rock burst origin prevention. *J. China Coal Soc.* **48**(5), 1861–1874. <https://doi.org/10.13225/j.cnki.jccs.2023.0158> (2023).
2. Khan, N. M. et al. Developing a new bursting liability index based on energy evolution for coal under different loading rates. *Sustainability* **14**(3), 1572. <https://doi.org/10.3390/su14031572> (2022).
3. Xu, Q. F. et al. Experimental study on impact failure characteristics of roadway with different ellipticity. *J. China Coal Soc.* **9**(1), 42 (2023).
4. Qiu, L. M. et al. Early-warning of rock burst in coal mine by low-frequency electromagnetic radiation. *Eng. Geol.* **279**, 105755. <https://doi.org/10.1016/j.enggeo.2020.105755> (2020).
5. Wang, K. & Du, F. Coal-gas compound dynamic disasters in China: A review. *Process Saf. Environ. Protect.* **133**, 1–17. <https://doi.org/10.1016/j.psep.2019.10.006> (2020).
6. Gao, M. S. et al. Graded support of rock burst roadway based on balance theory of impact energy and absorbed energy. *Rock Soil Mech.* **45**(01), 38–48. <https://doi.org/10.16285/j.rsm.2022.1834> (2024).
7. Tahmasebinia, F. et al. A novel damage model for strata layers and coal mass. *Energies* **13**(8), 1928. <https://doi.org/10.3390/en13081928> (2020).
8. Gale, W. J. A review of energy associated with coal bursts. *Int. J. Min. Sci. Technol.* **28**(5), 755–761. <https://doi.org/10.1016/j.ijmst.2018.08.004> (2018).
9. Yardimci, A. G. & Karakus, M. A new protective destressing technique in underground hard coal mining. *Int. J. Rock Mech. Min. Sci.* **130**, 104327. <https://doi.org/10.1016/j.ijrmms.2020.104327> (2020).
10. Pan, Y. S. et al. Study on safety of rockburst mine. *Journal of China Coal Society* **48**(05), 1846–1860. <https://doi.org/10.13225/j.cnki.jccs.2023.0294> (2023).
11. Pan, Y. S., Song, Y. M. & Liu, J. Pattern, change and new situation of coal mine rockburst prevention and control in China. *Chinese J. Rock Mech. Eng.* **42**(09), 2081–2095. <https://doi.org/10.13722/j.cnki.jrme.2022.1048> (2023).
12. Pan, Y. S., Xiao, Y. H. & Li, G. Z. Roadway hydraulic support for rockburst prevention in coal mine and its application. *J. China Coal Soc.* **45**(1), 90–99. <https://doi.org/10.13225/j.cnki.jccs.YG19.1762> (2020).
13. Afraei, S., Shahriar, K. & Madani, S. H. Developing intelligent classification models for rock burst prediction after recognizing significant predictor variables, Section 1. *Tunnell. Undergr. Space Technol.* **83**, 324–353. <https://doi.org/10.1016/j.tust.2018.09.022> (2019).
14. Askaripour, M. et al. Rockburst in underground excavations: A review of mechanism, classification, and prediction methods. *Undergr. Space* **7**(4), 577–607. <https://doi.org/10.1016/j.undsp.2021.11.008> (2022).
15. Pan, Y. S. et al. Research of hydraulic powered supports for entries' advanced support in fully-mechanized working face of rock burst mine. *Coal Sci. Technol.* **49**(6), 1–12. <https://doi.org/10.13199/j.cnki.cst.2021.06.001> (2021).
16. Wu, Y. P. et al. Structural design and motion response of parallelogram hydraulic support in pitching oblique mining face of steeply dipping coal seam. *Coal Sci. Technol.* **52**(04), 314–325. <https://doi.org/10.12438/cst.2023-1437> (2024).
17. Xiao, Y. H. et al. Buckling energy absorption reliability of energy absorption component of roadway rockburst preventing support. *J. Min. Saf. Eng.* **39**(02), 317–327. <https://doi.org/10.13545/j.cnki.jmse.2021.0495> (2022).
18. Zhang, J. Z. et al. Design of torsion plate energy-absorbing member and analysis of energy-absorbing and anti-impact characteristics. *Shock Vib.* **2023**(1), 8966724. <https://doi.org/10.1155/2023/8966724> (2023).

19. Wang, C. H. et al. Simulation and tests for new tubular type energy-absorbing and anti-impact members with stiffened plate under rock burst. *J. Vib. Shock* **38**(11), 203–210 (2019).
20. Pan, Y. S. *Rock Burst Engineering* (Higher Education Press, 2022).
21. Szurgacz, D. & Brodny, J. Analysis of the influence of dynamic load on the work parameters of a powered roof support's hydraulic leg. *Sustainability* **11**(9), 2570. <https://doi.org/10.3390/su11092570> (2019).
22. Masny, W. Powered support in dynamic load conditions-numerical analysis. *Arch. Min. Sci.* **65**(3), 453–468. <https://doi.org/10.24425/ams.2020.134129> (2020).
23. Pan, Y. S. et al. Study of tunnel support theory of rockburst in coal mine and its application. *J. China Coal Soc.* **39**(2), 222–228. <https://doi.org/10.13225/j.cnki.jccs.2013.2015> (2014).
24. Ma, X., Pan, Y. S. & Xiao, Y. H. Study on application of the mine anti-impact and energy-absorption device. *Appl. Mech. Mater.* **470**, 598–603. <https://doi.org/10.4028/www.scientific.net/AMM.470.598> (2014).
25. Xu, P., Shao, H. & Yan, J. L. Crashworthiness optimization design of expanding type energy absorption devices based on adaptive response surface method. *J. Vib. Shock* **36**(11), 118–123 (2017).
26. Wang, C. L. et al. Simulation and experiment study on energy absorption of a thin-walled tube component with vertical strip. *Int. J. Struct. Stabil. Dyn.* **23**(09), 2350103. <https://doi.org/10.1142/S0219455423501031> (2023).
27. Yao, R. Y. et al. On the crashworthiness of thin-walled multi-cell structures and materials: State of the art and prospects. *Thin-Walled Struct.* **189**, 110734. <https://doi.org/10.1016/j.tws.2023.110734> (2023).
28. Yao, R. Y. et al. A bio-inspired foam-filled multi-cell structural configuration for energy absorption. *Composit. Part B Eng.* **238**, 109801. <https://doi.org/10.1016/j.compositesb.2022.109801> (2022).
29. Xiang, X. M. et al. Sandwich structures with tapered tubes as core: A quasi-static investigation. *Defence Technol.* **33**, 447–462. <https://doi.org/10.1016/j.dt.2023.07.011> (2024).
30. Xiang, X. M. et al. The quasi-static compressive mechanical properties of barnacle bioinspired structures. *Eng. Struct.* **275**, 115307. <https://doi.org/10.1016/j.engstruct.2022.115307> (2023).
31. Xiang, X. M. et al. Finite element modeling for the simulation of the quasi-static compression of corrugated tapered tubes. *J. Visual. Exp.* **191**, 64708. <https://doi.org/10.3791/64708> (2023).
32. Xiao, X. C. et al. Experimental and numerical study on the energy absorption performance of aluminum foam-filled multi-cell square tubes. *Structures* **62**, 106250. <https://doi.org/10.1016/j.istruc.2024.106250> (2024).
33. Zhang, Q. & Zhang, R. X. Studies on the performance of impact resistant structure of hydraulic support in fully mechanized mining face under rock burst. *J. Theoret. Appl. Mech.* **60**(4), 649–658 (2022).
34. Guo, C. H., Mao, J. & Xie, M. Analysis of energy absorption characteristics of corrugated top beams of anti-impact hydraulic supports. *Alexandria Eng. J.* **61**(5), 3757–3772. <https://doi.org/10.1016/j.aej.2021.08.077> (2022).
35. Tian, L. Y. et al. Energy absorption performance of multicellular thin-walled energy-absorbing components of anti-shock support columns. *J. China Coal Soc.* **48**(05), 2224–2235. <https://doi.org/10.13225/j.cnki.jccs.2022.0903> (2023).
36. Pirmohammad, S. & Esmaili-Marzdashti, S. Multi-objective crashworthiness optimization of square and octagonal bitubal structures including different hole shapes. *Thin-Walled Struct.* **139**, 126–138. <https://doi.org/10.1016/j.tws.2019.03.004> (2019).
37. Gupta, P. K. & Gupta, N. K. A study of development mode of collapse with variation of strains and stresses during compression of metallic shells having dome-cone shape. *Thin-Walled Struct.* **126**, 68–78. <https://doi.org/10.1016/j.tws.2017.06.004> (2018).
38. Nikkha, H., Crupi, V. & Baroutaji, A. Crashworthiness analysis of bio-inspired thin-walled tubes based on Morpho wings microstructures. *Mech. Based Des. Struct. Mach.* **50**(10), 3683–3700 (2022).
39. Baroutaji, A. et al. Analysis and optimization of sandwich tubes energy absorbers under lateral loading. *Int. J. Impact Eng.* **82**, 74–88. <https://doi.org/10.1016/j.ijimpeng.2015.01.005> (2015).
40. Chen, Z. W. et al. Sensitivity analysis of the MIG welding process parameters based on response surface method. *J. Adhesion Sci. Technol.* **35**(6), 590–609. <https://doi.org/10.1080/01694243.2020.1816778> (2021).
41. Shi, X. Y. et al. Application of response surface analysis in the research on the green and rapid phosphating process. *China Surface Eng.* **36**(03), 223–234. <https://doi.org/10.11933/j.issn.1007-9289.2022022003> (2023).
42. Li, X. L. et al. Optimization of Srp/HAP for removal of fluoride, iron and manganese from groundwater in mining area by response surface methodology. *Coal Sci. Technol.* **51**(04), 231–238. <https://doi.org/10.13199/j.cnki.cst.2021-0686> (2023).
43. Upreti, H., Uddin, Z., Pandey, A.K., et al Sensitivity analysis for Sisko nanofluid flow through stretching surface using response surface methodology. *NANO* (2023) <https://doi.org/10.21203/rs.3.rs-3343783/v1>

Acknowledgements

This work was supported by the National Key Research and Development Program of China—Intelligent impact support technology and equipment for impact hazardous tunnels and engineering demonstration(2022Y-FC3004605).

Author contributions

Jianzhuo Zhang: Investigation, Resources, Writing—Original Draft, Funding acquisition. Fengnian Zhao(corresponding author): Formal analysis, Investigation, Writing—Original Draft. Hao Guo: Conceptualization, Supervision, Writing—Review & Editing. Chuanxu Wan: Methodology, Software, Visualization. Yonghui Xiao: Data Curation, Validation, Resources. All authors reviewed the manuscript.

Declarations

Competing interests

The authors declare no competing interests.

Additional information

Correspondence and requests for materials should be addressed to F.Z.

Reprints and permissions information is available at www.nature.com/reprints.

Publisher's note Springer Nature remains neutral with regard to jurisdictional claims in published maps and institutional affiliations.

Open Access This article is licensed under a Creative Commons Attribution-NonCommercial-NoDerivatives 4.0 International License, which permits any non-commercial use, sharing, distribution and reproduction in any medium or format, as long as you give appropriate credit to the original author(s) and the source, provide a link to the Creative Commons licence, and indicate if you modified the licensed material. You do not have permission under this licence to share adapted material derived from this article or parts of it. The images or other third party material in this article are included in the article's Creative Commons licence, unless indicated otherwise in a credit line to the material. If material is not included in the article's Creative Commons licence and your intended use is not permitted by statutory regulation or exceeds the permitted use, you will need to obtain permission directly from the copyright holder. To view a copy of this licence, visit <http://creativecommons.org/licenses/by-nc-nd/4.0/>.

© The Author(s) 2025